Research Article

3D Elbow Kinematics with Monoplanar Fluoroscopy: *In Silico* Evaluation

L. Tersi, S. Fantozzi, and R. Stagni

Department of Electronics, Computer Science and Systems (DEIS), University of Bologna, Via Venezia 52, I 47023 Cesena, Italy

Correspondence should be addressed to L. Tersi, luca.tersi@unibo.it

An *in-silico* assessment of the performance of 3D video-fluoroscopy for the analysis of the kinematics of long bones is proposed. A reliable knowledge of *in-vivo* joints kinematics in physiological conditions is fundamental in the clinical field. 3D video-fluoroscopy theoretically permits a mm/deg level of accuracy in joint motion analysis, but the optimization algorithm for the pose estimation is highly dependent on the geometry of the bone segment analyzed. An automated technique based on distance maps and tangency condition was applied to the elbow bones. The convergence domain was explored to quantify and optimize measurement accuracy in terms of bias and precision. By conditioning the optimization algorithm using simple image features, the estimation error had small dispersion (interquartile range within 0.5 and 0.025 mm/deg for out-of-plane and in-plane pose parameters, resp.), but with occasional bias and outliers. 3D video-fluoroscopy produced promising results for the elbow joint, but further *in-vitro* validation studies should be carried out.

1. Introduction

3D video-fluoroscopy is a technique for the evaluation of joint kinematics based on the alignment of 3D models of bones or prostheses and series of 2D radiographic images representing the relevant monoplanar or biplanar projections [1]. The joint kinematics is reconstructed calculating, independently for each video-frame, the 6 degrees of freedom (DOF) absolute pose (3 translations and 3 rotations) of each body segment, and then calculating the 6 DOFs of their relative pose.

Reliable knowledge of *in-vivo* joint kinematics, in physiological conditions, is fundamental for various clinical applications: (i) the study of prosthesis design must aim at the replication of intact joint biomechanical function [2, 3]; (ii) the development of quantitative diagnostic tools can help the detection of pathological alterations in motion [4], and (iii) the outcomes of orthopaedic surgery must be quantified to find correlation with the recovery of physiological joint motor activities [5, 6]. Moreover, from a methodological point of view, accurate methods are necessary to validate and to evaluate errors associated with non-invasive techniques

for the quantification of motion (i.e., inertial sensors, stereo-photogrammetry [7]). 3D video-fluoroscopy could provide this knowledge, because it theoretically permits to achieve a millimetre/degree accuracy level in joint motion analysis [8, 9], with relatively high dynamic performances (up to more than 50 fps with modern fluoroscopes), sufficient to analyze the motion during activities of daily living, and simple joint-specific tasks that can be performed inside the fluoroscopic volume (Figure 1).

In-vivo knee tasks, such as squat, stair climbing, chair raising and sitting or step up-down, were widely analysed with 3D video-fluoroscopy in replaced [10–13] and intact knee [14]. 3D video-fluoroscopy was also applied to quantify the *in-vivo* kinematics of ankle [15] and hip [16, 17] joints.

To estimate the 6 DOF of a bone segment in a frame acquired by video-fluoroscopy, a 3D model of the bone is virtually moved until it is best aligned to the relevant 2D image. This automatic procedure is typically carried out by means of an iterative optimization algorithms. Different metrics have been used to quantify a cost or a fitness function for the optimization such as: (i) the euclidean distance between the contour of the virtual projection of
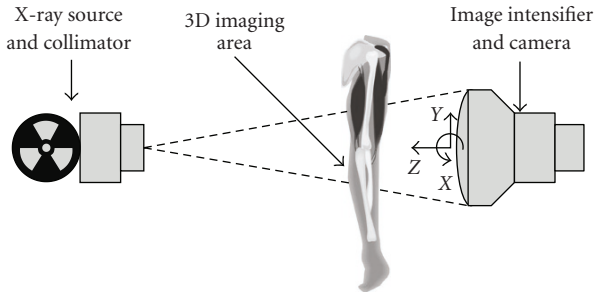
FIGURE 1: Configuration of a single-plane fluoroscopic acquisition system.

the model and the contour extracted from the fluoroscopic image [8, 18], (ii) the root mean square distance between the projection lines and the model surface [2], (iii) similarity measures between the fluoroscopic image and digitally reconstructed radiographies [19–23].

Promising accuracy levels have been reported for the intact knee joint: 0.23 mm for translation, 1.2 deg for rotation with biplanar fluoroscopy [22]; and 0.42 mm for in-plane and 5.6 mm for out-of-plane translations, 1.3 deg for rotation for monoplanar fluoroscopy [24]. However, these accuracies cannot a priori be considered valid for the other joints. Even if biplanar fluoroscopy is more robust, the present work focused on monoplanar fluoroscopy because it can investigate bigger volume with smaller X-ray dose for the patient.

The performance of 3D-fluoroscopy is affected by the geometry of the bone segments analysed, and its accuracy could vary considerably because local minima, caused by symmetries of the models surfaces, or by occlusions, could severely interfere with a correct estimation of the pose. Therefore, the technique is highly dependent on the initial guess of the pose for the optimization which is typically specified manually. However, the extent to which the intervention of the operator can affect the final reliability of the pose estimation has not been clarified yet. Therefore, 3D video-fluoroscopy might currently still be operator-dependent [18] and the application of 3D video-fluoroscopy is still too cumbersome to be suitable for routine clinical practice. The high potential of the method for routine clinical applications cannot be exploited without a concrete automation of the procedure, involving an automatic estimation of the initial guess of the pose. Therefore, the convergence domain of the optimization must be characterized in detail, exploring how different algorithms behave around reference poses.

Currently, no fluoroscopic methods have been applied to the *in-vivo* kinematics of the elbow joint. This joint has, however, been characterized *ex-vivo* [25], with Roentgen Stereophotogrammetric Analysis (RSA) [26, 27], and electromagnetic tracking systems [28], as well as *in-vivo* with noninvasive technique such as infrared stereo-photogrammetry [29], or nuclear magnetic resonance (MRI) [30]. Infrared stereo-photogrammetry, however, suffers accuracy limits due to soft tissue artifacts (20–48% of loss of rotational motion of the upper arm [31, 32]), while MRI fails to detect the effect of the active contribution of muscles to the motion. Even though fluoroscopy has not yet been applied to the elbow, this joint is of particular interest for its validation because it is characterized by (i) a high degree of bone superimposition, (ii) being composed by thin long bones (in contrast with the typical morphology of knee prosthesis), and (iii) marked longitudinal cylindrical symmetries (especially for the radius). These aspects make the fluoroscopic analysis of the intact elbow considerably difficult, thus particularly suitable for a validation study.

To significantly improve the quality and the robustness of 3D video-fluoroscopy, it is necessary to understand the effect of the various sources of errors on the final accuracy. For this purpose, an analytic approach is necessary in order to find appropriate solutions to each single defect of the method.

In the present study, we analysed, by means of computer simulation, the convergence property of a modified version of the pose estimation algorithm proposed by Lavalleé and Szelinsky [33] and based on adaptive distance maps (ADM), in order to better understand the influence of local minima and to optimize the pose estimation in terms of accuracy and precision. This algorithm was chosen because of its light computational weight and because it permits to achieve good accuracies even with incomplete contours [2], which can arise from occlusions or image blurring due to the bone motion.

In this evaluation study we considered (i) the geometric characteristic of the bone models, (ii) the resolution of the fluoroscopic projections, and (iii) the resolution of ADM as the only sources of errors. Confounding effects caused by the geometric distortions, by errors in the calibration of the fluoroscopic models, or by the incompleteness of the bone contours were disregarded in the present study.

The aim of the present study was to investigate the suitability of 3D video-fluoroscopy for the analysis of elbow bones kinematics, through a detailed exploration of the convergence domain of the minimization algorithm, in order to quantify and optimize measurement accuracy in terms of bias and precision.

2. Material and Methods

2.1. Pose Estimation Algorithm. An established technique was implemented to estimate the 3D pose of an object of known 3D geometry given its monoplanar fluoroscopic projection [2]. The algorithm was originally proposed by Lavallée and Szeliski [33] for biplanar projection, and is based on 3D adaptive distance maps. In brief, (i) the fluoroscope is virtually modelled with a perspective projection model; (ii) the 3D pose estimation is obtained with an iterative procedure that finds the best alignment between a bone surface model and its 2D fluoroscopic projection (typically a 1024×1024 DICOM image). In the present study, the bone surface was modelled with triangles meshes, however different representation can be used (i.e., cloud of points, NURBS). The resolution of the meshes was not relevant, because the images for the alignment were generated *in-silico* projecting exactly the same models. There was, thus, a perfect correspondence between the 3D model and the projection

independently from the meshes properties. The quality of the alignment is represented by a cost function defined as:

$$\text{RMSD}(p) = \sqrt{\frac{1}{n}\sum_{i=1}^{n}\left[d(S_m(p), l_i)\right]^2}. \quad (1)$$

RMSD is the root mean square distance between the surface $S_m(p)$ of the model m positioned in the pose $p = (Tx\ Ty\ Tz, \Theta x, \Theta y, \Theta z)$ and n projection lines l. The projection lines l represent the X-rays that generated the edge points of the bone segment projection extracted by a Canny edge detector [34] in the fluoroscopic image and is expressed in parametric form

$$l_i : C_i + \left(\frac{F - C_i}{L_i}\right)\lambda, \quad \lambda \in [0, L_i], \quad (2)$$

where $F = (F_x, F_y, F_z)$ is a point representing the X-ray source position (*focus*), $C_i = (C_{ix}, C_{iy}, C_{iz})$ is the ith of the n points of the contour, both expressed in the fluoroscopic system of reference, and L_i is their distance:

$$L_i = \|F - C_i\| \quad (3)$$

To quantify RMSD, l_i is sampled and, for each sampling point $P_k^i = l_i(\lambda_k)$, the distance from $S_m(p)$ is computed. The distance of the projection line from the surface is then defined as the minimum distance among those of the line sampling points:

$$d(S_m(p), l_i) = \min_k\left(d\left(S_m(p), P_k^i\right)\right). \quad (4)$$

The best alignment condition is finally identified finding the values of the pose p that minimize the RMSD with the Levenberg–Marquardt (LM) method [35]:

$$\text{RMSD}_{\min} = \min_p(\text{RMSD}(p)). \quad (5)$$

The VXL [36] implementation of LM was used in the present work.

For a faster quantification of the distance $d(S_m, l_i)$ between the line and the model surface, and to define the sampling step of l_i, adaptive distance maps (ADM) of the models surface were pre-computed and stored. Briefly, the ADM is an octree-based representation of an object [37]. In this representation, the volume outside and inside the surface of the object is non-uniformly discretized. The map assigns to each point of the discretization the corresponding signed distance from the surface of the model: positive if outside, negative if inside the object. The distance is computed as the minimum distance between the discretization point and the surface of model of the bone. The structure of the ADM is an octree which is built with an iterative procedure which subdivides a cube (also called octant) iteratively in other 8 half-side octants only if it contains at least one point of the mesh. The octree is then refined to avoid discontinuities between the levels of subdivision of two adjacent octants. The vertices of the octants are the volume discretization points. The distance of a generic point from the surface is then computed with a tri-linear interpolation of the distances of the 8 vertices of the smallest octant containing the point. The octant side dimension gets smaller closer to the surface, thus the interpolation error becomes negligible. In the present work, the resolution of the octree (smallest octant side) will be referred as DMR (Distance Map Resolution). For a further improvement of the algorithm speed, also the sampling step of the projection lines is adaptive. The sampling step varies accordingly to the local resolution of the ADM and gets smaller closer to the surface. If s_k^i is the side of the smallest octant containing the sampled point P_k^i then the next point to evaluate the distance will be

$$
\begin{aligned}
P_{k+1}^i &= l_i(\lambda_{k+1}), \\
\lambda_{k+1} &= \lambda_k + \frac{s_k^i}{2}.
\end{aligned}
\quad (6)
$$

Finally, l_i is resampled around the closest point to the surface with a uniform step length ten times smaller than DMR.

A global reference frame was defined with the x and y axis parallel and z-axis perpendicular to the image plane, with the origin in the centre of the image plane. The Euler zxy convention was used for rotations. The field of view was represented with a diameter of 400 mm. The X-ray source was virtually placed in $F = (0, 0, 1000)$ mm, representing a typical distance of a standard fluoroscope, and pixel spacing was fixed at 0.34 mm. The effects on the final accuracy of the errors associated to the identification of the principal point (xy-coordinates of the X-ray source) and principal distance (z-coordinate of the X-ray source) were disregarded in the present study as already quantified elsewhere [38]. The X-rays were represented by a beam of straight lines and the effect of the geometrical image distortions, caused by the electronics of the image formation chain of real fluoroscopes [39], was not considered in the present study because, dealing with real images, the geometrical distortion can be efficiently corrected using a global spatial warping techniques [40, 41].

In the implementation of the LM minimization algorithm, 3 parameters must be specified: (i) the convergence tolerance on the RMSD (f_{tol}), (ii) the convergence tolerance on the 6 DOF of the pose p (x_{tol}), and (iii) the step length for forward (FD) Jacobian computation (eps).

2.2. Algorithm Convergence Properties. High resolution models of humerus, ulna, and radius were downloaded from the official site of the European project VAKHUM (contract #IST-1999-10954 [42]) and used in the performed simulations. For each model two ADM were calculated and stored with DMR equal to 0.5 and 1 mm.

An anatomical reference frame was associated to each bone model according to the ISB recommendations [43]. Each model was then placed in a reference pose (parallel to xy-plane, lateral view, out of plane translation $Tz = 200$ mm) simulating a typical fluoroscopic frame. Flat shaded projections were generated and the complete contour was extracted and then used for the alignment (Figure 2).

The sensitivity of the cost function to each DOF of p was analysed. The RMSD function was evaluated keeping 5 DOF constant and varying a single DOF at a time, with
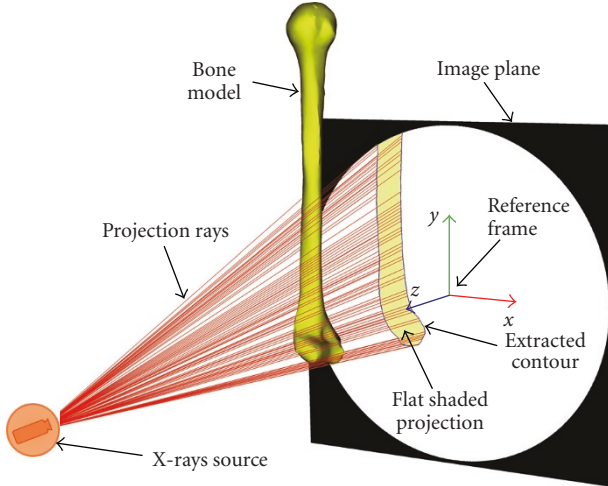
FIGURE 2: Perspective projection model. The bone model is placed in a reference position and a flat shaded projection is generated. The contour points are extracted and the projection lines are back projected towards the X-rays source.

a step of 0.1 mm/deg, around the reference pose, from -30 to 30 mm/deg for translations and rotations, respectively. The analysis was repeated for humerus, ulna and radius. This permitted to evaluate how the shape and the symmetry of the different bone models influence the minimization. The RMSD with respect to each DOF analysed, can be represented as a cusp. The sensitivity (S) of RMSD to the variation of the pose parameters, was defined as the average absolute slope between the left and the right tangents of the curve around its minimum (Figure 3):

$$S_p = \frac{1}{2} \left(\left| \frac{\mathrm{RMSD}(p_m) - \mathrm{RMSD}(p_m + \Delta p)}{\Delta p} \right| \\ + \left| \frac{\mathrm{RMSD}(p_m) - \mathrm{RMSD}(p_m - \Delta p)}{\Delta p} \right| \right), \quad (7)$$

where p_m is the value of the generic pose parameter p correspondent to the minimum of RMSD.

A detailed convergence domain analysis was carried out for different sets of simulation parameters. The minimization was started from 1000 randomly-chosen initial-condition poses among 117649 permutations obtained varying the translations (ΔTx, ΔTy, ΔTz) and rotations ($\Delta \Theta x$, $\Delta \Theta y$, $\Delta \Theta z$) between the values -10, -7, -3, 0, 3, 7, 10 mm/deg, respectively, around the reference pose. The simulations parameters were initially varied using different values for DMR (0.5–1 mm), and eps (10^{-1}–10^{-4} mm/deg) while x_{tol} and f_{tol} were both kept fixed at 10^{-3} mm/deg.

2.3. Algorithm Conditioning. Different authors stressed that the minimization of RMSD is affected by local minima and by the large differences in the sensitivity to the various DOF [13, 24]. If the minimization starts from initial conditions inside a local minima basin, the pose estimation will be incorrect. Two different solutions were implemented and

compared in order to better deal with the problem of local minima.

The first, proposed by Fregly et al. [24], involved the sequential (*seq*) minimization of the DOF in order of sensitivity. For this purpose, three groups of DOF were formed: (i) in-plane pose parameters (Tx, Ty, Θz); (ii) out-of-plane rotations (Θx, Θy); (iii) out-of-plane translation (Tz). After this three sequential minimization, the RMSD was finally further minimized with respect to the 6 DOF simultaneously.

The second solution (*feat*) involved the use of features extracted from the image to get closer to the real pose before starting the minimization. Two features were calculated on the bone-contour points: (i) the direction of maximum variance of the distribution, and (ii) the farthest point from the field of view border among the projections of the bone-contour point along the maximum variance axis. The first feature was used to evaluate a first guess for the bone model orientation around the projection axis (Θz) , while the in-plane translation components (Tx, Ty) were estimated using the second feature. The three DOF were modified iteratively until convergence, and then the minimization was started as previously described.

The analysis was repeated for each bone model, using *seq*, *feat* and *seq-feat* together, with 2 values of eps (10^{-1}–10^{-4} mm/deg) and DMR = 0.5 mm.

2.4. Data Analysis. For each set of parameters, the final deviations between estimated and reference poses, and the relevant residual RMSD were quantified. Bias and precision of the final estimates of the pose were quantified calculating for each DOF the median (m) and the interquartile range (iqr). For bias results, a Student's t-test ($P < .05$) was performed to determine if the values were statistically different from zero, indicating the presence of a systematic error. Moreover, to measure how outlier-prone the distributions were, the kurtosis (k) was also calculated.

To investigate the effects of the different minimization parameters (DMR, eps, *seq*, *feat*, bone models and initial deviations) on the final estimates and RMSD, an n-way analysis of variance (ANOVA) was performed considering a significance level $\alpha = 0.05$ (with Bonferroni adjustment for multiple comparisons).

3. Results

3.1. Sensitivity Analysis. The cusp shape of RMSD with respect to each DOF, except Tz, was verified, while with respect to Tz, RMSD showed a rounder trend. In particular the trend of the cost function for the humerus is shown in Figure 3. Similar trends were obtained also for the ulna and the radius models.

For all the bone models analysed, the sensitivity analysis highlighted the presence of an evident global minimum in correspondence of the reference pose ($\Delta Ti = 0$ and $\Delta \theta i = 0$, $i= x$, y, z). This was true for all the 6 DOF but with higher sensitivity for the in-plane DOF, see Table 1. In particular, the highest sensitivity was obtained
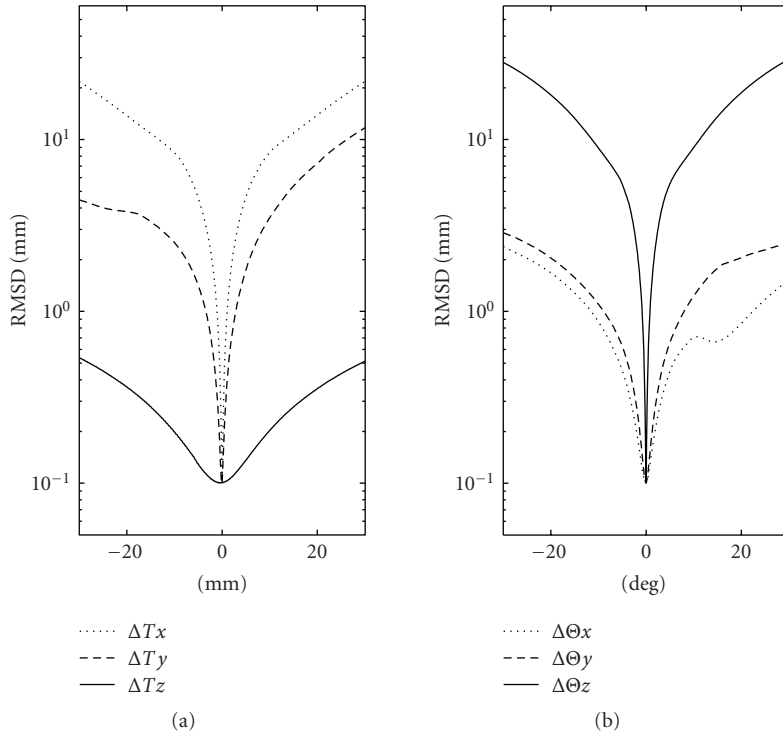
FIGURE 3: The root mean square distance RMSD plotted against the perturbation on the translations (a) and rotations (b) for the humerus bone. The RMSD forms a cusp around its minimum.

for Θz (mean value $8.5e-1$ mm $\cdot$ deg^{-1}) while the smallest was obtained for Tz (mean value $1.2e-3$ mm $\cdot$ mm^{-1}). A clear local minimum, however, is shown for the humerus at approximately $\Delta\theta x = 15$ deg (Figure 3), but was not found for the other bone models. All the sensitivity values of the radius, excepted S_{Tx} and $S_{\theta z}$, were approximately one order of magnitude smaller than those of ulna and humerus. The RMSD versus ΔTy was asymmetric: since the analysed bone models were defined with the epicondyles in the middle of the imaging field, the RMSD grew faster when the model is moved further out of the imaging field ($\Delta Ty > 0$ mm), slower in the opposite direction. The same behaviour was found also for ulna and radius, but, since the bone models were defined in the opposite part of the imaging field, the RMSD grew faster in the opposite direction, thus for $\Delta Ty < 0$ mm.

3.2. Distance Map Resolution. Results of the convergence domain analysis without conditioning (DMR = 1 mm and 0.5 mm; eps = 10^{-4} mm/deg) showed that a median error lower than 1 mm/deg was produced for each bone model and each DOF. The distributions, however, had large dispersions especially for Tz and Θx ($iqr > 5$ mm/deg). Nevertheless, also for the other DOF we found numerous outliers: k ranged from a minimum of 8 (Ty of the radius, DMR = 0.5 mm) to a maximum of 866 (Θz of the radius, DMR = 1 mm). For all three bone models, with eps = 10^{-1} mm/deg, the *iqr* was larger than 1 mm/deg for in plane DOF and Θy, and larger than 10 mm/deg for Θx and Tz. Generally, for all three

models and both values of eps, the interquartile ranges were always smaller when using a DMR = 0.5 mm rather than 1 mm ($P < .05$). We report in Table 2 the results obtained for the radius, representing the most problematic case.

3.3. Sequential Alignment. The sequential alignment with DMR = 0.5 mm slightly decreased the number of local minima and outliers identified by the LM algorithm (Figure 4): k ranged from a minimum of 1.4 (Tx of the ulna, eps = 10^{-4} mm) to a maximum of 265 (Tz of the humerus, eps = 10^{-4} mm). The mean value of k between the models and the DOF was equal to 31 for eps = 10^{-4} mm, and equal to 25 for eps = 10^{-1} mm.

Using eps = 10^{-4} mm/deg, the optimization of $Tx,$ Θz and Θy resulted in median < 0.04 mm/deg, iqr < 0.10 mm/deg even if Θy had a large number of outliers. Ty had a median < 0.1 mm/deg, with iqr < 0.50 mm/deg: Figure 4 shows the outliers gathered together only for positive values of Ty. Especially for the radius, the minimization process of Θx and Tz tended to prematurely stop during its descent towards the global minimum, resulting in large dispersions (median < 0.05 mm/deg, $iqr = 5.10$ deg and $iqr = 4.10$ mm, respectively).

Increasing the step eps to 10^{-1} mm/deg, for all the three models, the median values for Θx and Tz were smaller than 0.08 mm/deg, with a dispersion lower than 0.45 mm/deg.

3.4. Features. A further reduction of the number of outliers was introduced by the use of features to estimate an initial

TABLE 1: Sensitivity of the RMSD to the variation of the 6 DOF.

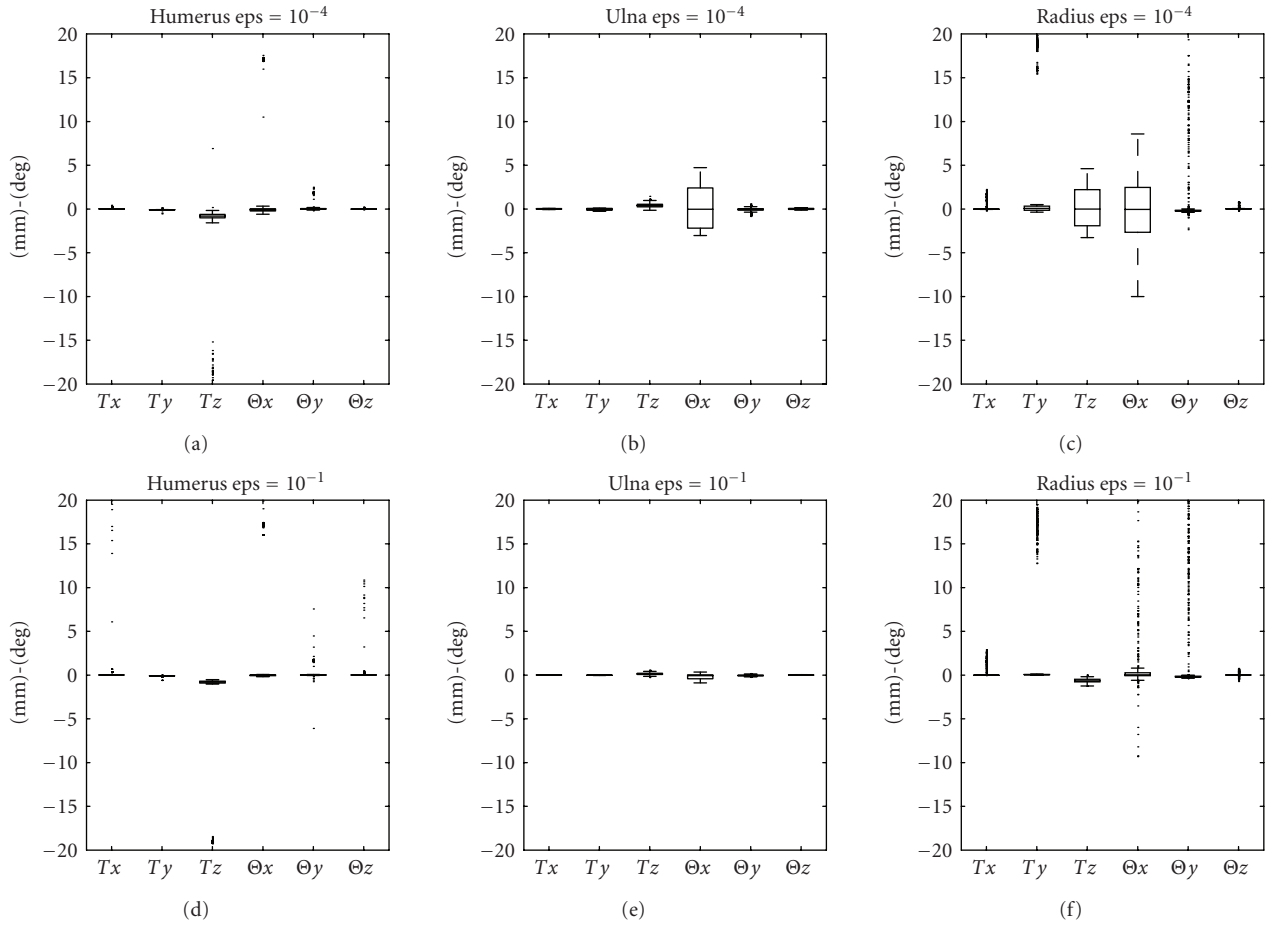| Model	S_{Tx} [mm·mm^{-1}]	S_{Ty} [mm·mm^{-1}]	S_{Tz} [mm·mm^{-1}]	$S_{\Theta x}$ [mm·deg^{-1}]	$S_{\Theta y}$ [mm·deg^{-1}]	$S_{\Theta z}$ [mm·deg^{-1}]
humerus	$5.5e{-}1$	$9.6e{-}2$	$1.5e{-}3$	$8.2e{-}3$	$1.6e{-}2$	$8.0e{-}1$
radius	$5.7e{-}1$	$7.6e{-}2$	$0.5e{-}3$	$1.0e{-}3$	$0.3e{-}2$	$9.2e{-}1$
ulna	$5.3e{-}1$	$1.6e{-}1$	$1.5e{-}3$	$5.0e{-}3$	$2.0e{-}2$	$8.4e{-}1$

FIGURE 4: Box and whisker plots of the *seq* alignment with DMR = 0.5, (panels a, b, c) eps = 10^{-4} mm/deg, or eps = 10^{-1} mm/deg (panels d, e, f).

TABLE 2: Effects of the distance map resolution on the pose parameters estimates for the radius model.

DOF	DMR = 1 mm			DMR = 0.5 mm		
	m	iqr	k	m	iqr	k
Tx [mm]	-0.03	0.01	20.2	-0.02	0.01	50.7
Ty [mm]	0.26	0.75	8.4	0.21	0.48	9.7
Tz [mm]	0.79	7.15	16.6	-0.2	4.41	47.3
Θx [deg]	-0.05	8.5	76.8	-0.11	5.5	74.1
Θy [deg]	-0.22	0.12	140.2	-0.19	0.1	293.7
Θz [deg]	0.02	0.02	307.8	0.01	0.02	866.2

guess for the in-plane DOF, (Figure 5). As for the sequential alignment, the use of a big step (eps = 10^{-1}) for the FD Jacobian computation, increased the precision of the

estimations of Θx and Tz (for the radius iqr = 0.31 deg and iqr = 0.24 mm, resp.). The estimation of Tz was biased for the humerus and radius with medians approximately equal to -0.7 mm, as was Θy of the radius (median equal to 0.2 deg), while for the other DOF and for the ulna the median values were always lower than 0.01 mm/deg. Considering the humerus and both the values of eps, the LM algorithm sometimes converged to the local minimum shown in Figure 5 ($Tz \approx -18$ mm, $\Theta x \approx +18$ mm), keeping the value of k high (medium values: 62 for the humerus, 2.8 for the ulna, 3.3 for the radius).

3.5. Features and Sequential Alignment. The simultaneous use of *feat* and *seq* had no significant effect on the final RMSD, nor on the errors of the single DOF estimates ($P >$ .05). The final results obtained for humerus, ulna and radius
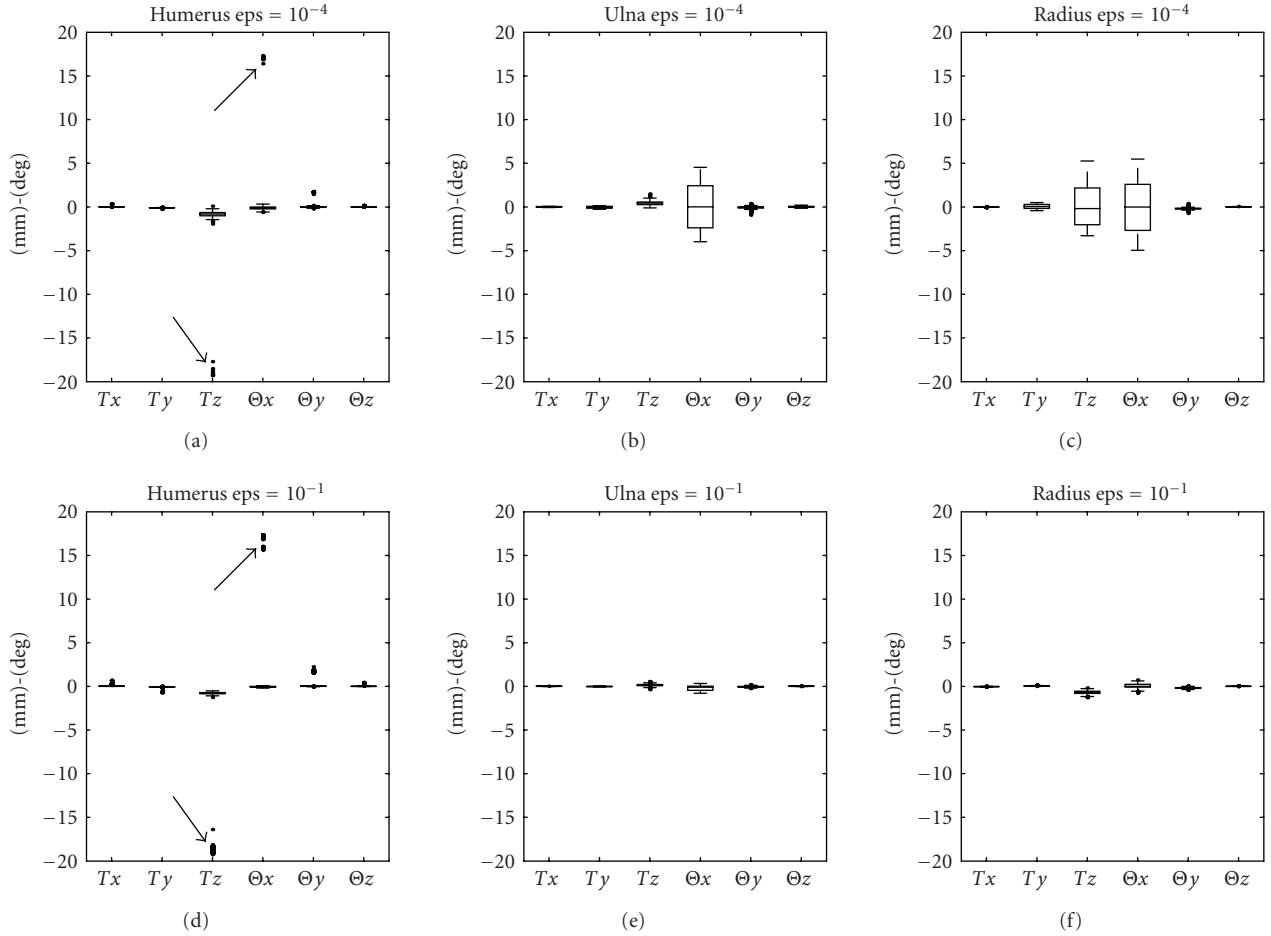
FIGURE 5: Box and whisker plots of the *feat* alignment with DMR = 0.5, (panels a, b, c) eps = 10^{-4} mm/deg, or eps = 10^{-1} mm/deg (panels d, e, f).

with eps = 10^{-1} mm/deg, and DMR = 0.5 mm are reported in Table 3. The *t*-test showed that the final estimates were always statistically different from 0, thus biased.

4. Discussion

In this work, a sensitivity analysis and a convergence domain analysis of the minimization algorithm for the pose estimation in 3D video-fluoroscopy were addressed.

The sensitivity analysis showed that the cost function (RMSD) varies differently with each DOF: the in-plane pose parameters have a sensitivity at least one order of magnitude larger than the out-of-plane pose parameters. Moreover, the performed simulation showed that the cost function could have different behaviours depending on the analysed segment (Figure 3): considering Θx, we found a clear local minimum for the humerus but not for ulna and radius. For all three models, the RMSD with respect to Ty showed an asymmetric trend. That is due to the fact that only a partial part of the bone is included in the imaging field (Figure 2), thus, given the long diaphysis of the bone, two different scenarios occur while moving the model along the y-axis: if the models moves further into the imaging field,

the projection lines coming from the bone contour points intersect or pass near to the model surface, continuing to give only a little contribution to the increment of the cost function. On the other hand, if the model moves further out of the imaging field, there is no model surface for part of the projection lines to intersect with, increasing their contribution to the cost function. The findings about the RMSD explained the behaviour of the unconditioned LM algorithm, which was found to be noticeably sensitive to the local minima of the RMSD. Given the longitudinal cylindrical symmetry, the estimations of the pose of long bones were affected by large dispersions not only for Tz, as previously thoroughly reported for the knee prostheses, but also for Θx (see Table 2). Moreover, for the DOF with relative small *iqr* such as the in-plane pose parameters, the values of k were high (>8), that is the distributions were affected by large number of outliers. The ANOVA confirmed the hypothesis that the higher is the resolution of the distance map (DMR) the more the accuracy and the precision of the technique increase ($P < .05$). However, given the limits of the resolution of the fluoroscopic image and of the surface model mesh, a further increasing of DMR would be unnecessary. For the unconditioned minimization, varying the step for the

TABLE 3: Final accuracy in terms of median (m), interquartile range (iqr) and kurtosis (k) of the pose estimations, for the three bone models with the *seq-feat* alignment.

DOF	Humerus			Ulna			Radius		
	m	iqr	k	m	iqr	k	m	iqr	k
Tx [mm]	0.003	0.004	14.0	0.005	0.008	3.0	−0.021	0.006	4.8
Ty [mm]	−0.087	0.005	73.7	−0.018	0.025	2.2	0.051	0.025	3.1
Tz [mm]	−0.766	0.153	5.0	0.132	0.155	3.3	−0.692	0.260	3.1
Θx [deg]	−0.045	0.090	4.9	−0.071	0.474	2.0	0.017	0.317	3.1
Θy [deg]	0.011	0.032	5.6	−0.044	0.086	3.2	−0.195	0.073	4.2
Θz [deg]	0.001	0.011	26.8	0.007	0.019	2.9	0.007	0.003	4.9

FD Jacobian computation (eps) from 10^{-4} to 10^{-1} mm/deg induced a further instability.

To solve the convergence problems of the LM algorithm, the effect of the *seq* alignment on the minimization process was evaluated. When the initial conditions are too far from the reference pose, if not conditioned, the pure algorithm tries to explore the value of the cost function varying all the 6 DOF simultaneously, risking to move the less sensitive DOF away from the global solution. With the *seq* alignments, instead, the DOF with larger convergence domain are aligned in a first step, while the more critical (out-of-plane) DOF are minimized only when closed to the reference pose. Although this technique leads to an improvement of the precision of the estimate (Figure 4), the algorithm is still sensitive to local minima, or to local low-sensitivity areas of the cost function that can occur also for the in-plane pose parameters, such as for Ty (Figure 3). This could be the cause for the still high number of outliers (mean of $k > 25$) obtained with the *seq* alignment. Varying eps from 10^{-4} to 10^{-1} mm/deg permitted to improve the performance of the optimization avoiding the early convergence for the less sensitive DOF (Tz and Θx, Figure 4). However the problems of convergence are not completely solved, probably because two different DOF could have a correlated effect on the RMSD, thus, a sequential minimization could interfere with a proper descending to the global minimum.

The use of features completely avoided the problems of the *seq* alignment, because, differently from *seq*, the *feat* alignment is completely independent from the RMSD and, thus, from its local minima. For our simulations, we used two simple features: (i) the direction of maximum variance of the distribution of bone-contour points to extrapolate Θz, and (ii) a characteristic point such as the farthest from the field of view border for Tx, Ty. These features are particularly suitable for long bones, which cannot be completely included in the field of view; for short bones or prosthesis, however, the mean of the coordinates of the contour points can equally be used. These minimization settings, together with a FD Jacobian step eps = 10^{-1} (bigger enough to filter small noisy fluctuation of the RMSD), permitted to significantly reduce m, iqr, and k.

Even if the combined effects of *feat* and *seq* did not introduced further improvements (P-value > .05), with a fine tuning of the minimization parameters, a high level of precision can be achieved ($iqr < 0.025$ mm/deg for in-plane pose parameters, $iqr < 0.5$ mm/deg for out-of-plane pose parameters) but with a high variability between the models (i.e., considering Θx, iqr equal to 0.09 deg for the humerus, and equal to 0.47 deg for the ulna), confirming the hypothesis that the performances of the method should be assessed for each bone model to be analysed. The results also showed that the final estimate is biased. This is due to the intrinsic limitations of the technique given by the resolution of the fluoroscopic projections and of the distance maps. Moreover, in spite of the fine tuning of the optimization parameters, the local minima showed in Figure 3 of the RMSD versus Θx for the humerus, seldom caused the LM minimization algorithm to detect false poses. These false poses can generally be easily identified by an operator with a visual feedback of the alignment and, in such cases, the minimization can be repeated starting from a different initial condition.

The results of this study confirm that the accuracy and the precision that can be achieved, especially with the *feat* alignment, allow the technique to be suitable for the kinematic study of the elbow, but without excluding the complete independence by the operator.

5. Conclusions

In the present work, we proposed an analytical process to evaluate the performance of 3D video-fluoroscopy for its application to the analysis of kinematics of long bones, by means of *in-silico* simulations. The effects of the dominant sources of error such as bone symmetries, distance map resolution and image spacing, were investigated. Solutions were proposed to improve the accuracy and the precision of the method.

Given the high variability of the morphology of the bones or prostheses that could be analysed with 3D video-fluoroscopy, different performance assessment studies should be carried out before undertaking any new application of the technique, especially for clinical purpose. We focused on the elbow because it allowed to investigate different characteristics of 3D video-fluoroscopy applied to long bones. Compared to knee prosthesis, which have been deeply studied during the past years with 3D fluoroscopy [10–12], the marked cylindrical longitudinal symmetries of long bones constitute a dominant disturbing factor that could interfere with the final accuracy of the technique.

FIGURE 6: Real fluoroscopic image of the elbow: note the superimposition of bones and the low-contrast contours and the results of the Canny edge detection for the humerus.

The robustness of the alignment algorithm applied to the elbow joint was completely characterized. Even if the convergences to local minima was not completely avoided, with a proper conditioning and a fine tuning of the minimization algorithm parameters, excellent results can be achieved in term of low bias and high precision. Moreover, the methods and the findings addressed in this work focusing on monoplanar projections, can easily be extended also to biplanar 3D video-fluoroscopy.

In order to achieve a complete automation of the pose estimation algorithm, the problem of local minima should be completely solved. Robust optimization algorithms based on simulated annealing [13] or on Unscented Kalman Filtering [44] have been proposed. These techniques will be implemented and evaluated in future works in combination with the conditioning of minimization based on *feat* and *seq* which was proven to effectively improve the performance of LM. However, the bias errors committed will not be avoided with either of these robust techniques, because the errors are due to characteristics intrinsic to the monoplanar fluoroscopic analysis. Furthermore, when considering other sources of error typical of real fluoroscopic sessions such as the geometric distortions, surface model inaccuracies, errors in the calibration of the fluoroscopic models, and incompleteness of the bone contours, the accuracy would certainly worsen (**Figure 6**).

Again, all these considerations are to confirm that for application to the kinematics of any particular joint, a detailed validation study should be carried out, especially for clinical studies. The accuracy and the precision achieved with the *feat* alignment, allow the technique to be suitable for the kinematic study of the elbow, and most likely even of other long bones, however further *in-vitro* validation must be carried out.

References

[1] R. Stagni, S. Fantozzi, A. G. Cutti, and A. Cappello, "Kinematic analysistechniques and their application in biomechanics," in *Biomedical Systemtechnolog: Muscular Skeletal System*, C. Leondes, Ed., vol. 4, pp. 135–183, World Scientific, 2009.

[2] S. Zuffi, A. Leardini, F. Catani, S. Fantozzi, and A. Cappello, "A model-based method for the reconstruction of total knee replacement kinematics," *IEEE Transactions on Medical Imaging*, vol. 18, no. 10, pp. 981–991, 1999.

[3] S. Hirokawa, M. Abrar Hossain, Y. Kihara, and S. Ariyoshi, "A 3D kinematic estimation of knee prosthesis using X-ray projection images: clinical assessment of the improved algorithm for fluoroscopy images," *Medical and Biological Engineering and Computing*, vol. 46, no. 12, pp. 1253–1262, 2008.

[4] P. M. Ludewig and J. F. Reynolds, "The association of scapular kinematics and glenohumeral joint pathologies," *Journal of Orthopaedic & Sports Physical Therapy*, vol. 39, no. 2, pp. 90–104, 2009.

[5] S. Tashman, P. Kolowich, D. Collon, K. Anderson, and W. Anderst, "Dynamic function of the ACL-reconstructed knee during running," *Clinical Orthopaedics and Related Research*, vol. 454, pp. 66–73, 2007.

[6] D. A. Dennis, M. R. Mahfouz, R. D. Komistek, and W. Hoff, "In vivo determination of normal and anterior cruciate ligament-deficient knee kinematics," *Journal of Biomechanics*, vol. 38, no. 2, pp. 241–253, 2005.

[7] A. Cappello, R. Stagni, S. Fantozzi, and A. Leardini, "Soft tissue artifact compensation in knee kinematics by double anatomical landmark calibration: performance of a novel method during selected motor tasks," *IEEE Transactions on Biomedical Engineering*, vol. 52, no. 6, pp. 992–998, 2005.

[8] S. A. Banks and W. A. Hodge, "Accurate measurement of three-dimensional knee replacement kinematics using single-plane fluoroscopy," *IEEE Transactions on Biomedical Engineering*, vol. 43, no. 6, pp. 638–649, 1996.

[9] J. B. Stiehl, R. D. Komistek, D. A. Dennis, R. D. Paxson, and W. A. Hoff, "Fluroscopic analysis of kinematics after posterior-cruciate-retaining knee arthroplasty," *The Journal of Bone and Joint Surgery. British*, vol. 77, no. 6, pp. 884–889, 1995.

[10] S. Fantozzi, A. Leardini, S. A. Banks, M. Marcacci, S. Giannini, and F. Catani, "Dynamic in-vivo tibio-femoral and bearing motions in mobile bearing knee arthroplasty," *Knee Surgery, Sports Traumatology, Arthroscopy*, vol. 12, no. 2, pp. 144–151, 2004.

[11] D. A. Dennis, R. D. Komistek, M. R. Mahfouz, B. D. Haas, and J. B. Stiehl, "Multicenter determination of in vivo kinematics after total knee arthroplasty," *Clinical Orthopaedics and Related Research*, no. 416, pp. 37–57, 2003.

[12] S. A. Banks, G. D. Markovich, and W. A. Hodge, "In vivo kinematics of cruciate-retaining and -substituting knee arthroplasties," *The Journal of Arthroplasty*, vol. 12, no. 3, pp. 297–304, 1997.

[13] M. R. Mahfouz, W. A. Hoff, R. D. Komistek, and D. A. Dennis, "A robust method for registration of three-dimensional knee implant models to two-dimensional fluoroscopy images," *IEEE Transactions on Medical Imaging*, vol. 22, no. 12, pp. 1561–1574, 2003.

[14] R. D. Komistek, D. A. Dennis, and M. Mahfouz, "In vivo fluoroscopic analysis of the normal human knee," *Clinical Orthopaedics and Related Research*, no. 410, pp. 69–81, 2003.

[15] R. D. Komistek, J. B. Stiehl, F. F. Buechel, E. J. Northcut, and M. E. Hajner, "A determination of ankle kinematics using

fluoroscopy," *Foot and Ankle International*, vol. 21, no. 4, pp. 343–350, 2000.

[16] D. A. Dennis, R. D. Komistek, E. J. Northcut, J. A. Ochoa, and A. Ritchie, ""In vivo" determination of hip joint separation and the forces generated due to impact loading conditions," *Journal of Biomechanics*, vol. 34, no. 5, pp. 623–629, 2001.

[17] R. D. Komistek, D. A. Dennis, J. A. Ochoa, B. D. Haas, and C. Hammill, "In vivo comparison of hip separation after metal-on-metal or metal-on-polyethylene total hip arthroplasty," *The Journal of Bone and Joint Surgery. American*, vol. 84, no. 10, pp. 1836–1841, 2002.

[18] W. A. Hoff, R. D. Komistek, D. A. Dennis, S. M. Gabriel, and S. A. Walker, "Three-dimensional determination of femoral-tibial contact positions under in vivo conditions using fluoroscopy," *Clinical Biomechanics*, vol. 13, no. 7, pp. 455–472, 1998.

[19] D. Tomazevic, B. Likar, T. Slivnik, and F. Pernus, "3-D/2-D registration of CT and MR to X-ray images," *IEEE Transactions on Medical Imaging*, vol. 22, no. 11, pp. 1407–1416, 2003.

[20] D. B. Russakoff, T. Rohlfing, K. Mori, et al., "Fast generation of digitally reconstructed radiographs using attenuation fields with application to 2D-3D image registration," *IEEE Transactions on Medical Imaging*, vol. 24, no. 11, pp. 1441–1454, 2005.

[21] P. W. de Bruin, B. L. Kaptein, B. C. Stoel, J. H. C. Reiber, P. M. Rozing, and E. R. Valstar, "Image-based RSA: roentgen stereophotogrammetric analysis based on 2D-3D image registration," *Journal of Biomechanics*, vol. 41, no. 1, pp. 155–164, 2008.

[22] B.-M. You, P. Siy, W. Anderst, and S. Tashman, "In vivo measurement of 3-D skeletal kinematics from sequences of biplane radiographs: application to knee kinematics," *IEEE Transactions on Medical Imaging*, vol. 20, no. 6, pp. 514–525, 2001.

[23] W. Anderst, R. Zauel, J. Bishop, E. Demps, and S. Tashman, "Validation of three-dimensional model-based tibio-femoral tracking during running," *Medical Engineering & Physics*, vol. 31, no. 1, pp. 10–16, 2009.

[24] B. J. Fregly, H. A. Rahman, and S. A. Banks, "Theoretical accuracy of model-based shape matching for measuring natural knee kinematics with single-plane fluoroscopy," *Journal of Biomechanical Engineering*, vol. 127, no. 4, pp. 692–699, 2005.

[25] H. E. J. Veeger, B. Yu, K.-N. An, and R. H. Rozendal, "Parameters for modeling the upper extremity," *Journal of Biomechanics*, vol. 30, no. 6, pp. 647–652, 1997.

[26] A. Ericson, A. Arndt, A. Stark, P. Wretenberg, and A. Lundberg, "Variation in the position and orientation of the elbow flexion axis," *The Journal of Bone and Joint Surgery. British*, vol. 85, no. 4, pp. 538–544, 2003.

[27] D. Eygendaal, E. R. Valstar, J. O. Söjbjerg, and P. M. Rozing, "Biomechanical evaluation of the elbow using roentgen stereophotogrammetric analysis," *Clinical Orthopaedics and Related Research*, no. 396, pp. 100–105, 2002.

[28] F. Schuind, S. O'Driscoll, S. Korinek, K. N. An, and B. F. Morrey, "Loose-hinge total elbow arthroplasty: an experimental study of the effects of implant alignment on three-dimensional elbow kinematics," *The Journal of Arthroplasty*, vol. 10, no. 5, pp. 670–678, 1995.

[29] R. Schmidt, C. Disselhorst-Klug, J. Silny, and G. Rau, "A marker-based measurement procedure for unconstrained wrist and elbow motions," *Journal of Biomechanics*, vol. 32, no. 6, pp. 615–621, 1999.

[30] A. Goto, H. Moritomo, T. Murase, et al., "In vivo elbow biomechanical analysis during flexion: three-dimensional motion analysis using magnetic resonance imaging," *Journal of Shoulder and Elbow Surgery*, vol. 13, no. 4, pp. 441–447, 2004.

[31] A. G. Cutti, G. Paolini, M. Troncossi, A. Cappello, and A. Davalli, "Soft tissue artefact assessment in humeral axial rotation," *Gait & Posture*, vol. 21, no. 3, pp. 341–349, 2005.

[32] R. Stagni, S. Fantozzi, A. Cappello, and A. Leardini, "Quantification of soft tissue artefact in motion analysis by combining 3D fluoroscopy and stereophotogrammetry: a study on two subjects," *Clinical Biomechanics*, vol. 20, no. 3, pp. 320–329, 2005.

[33] S. Lavallee and R. Szeliski, "Recovering the position and orientation of free-form objects from image contours using 3D distance maps," *IEEE Transactions on Pattern Analysis and Machine Intelligence*, vol. 17, no. 4, pp. 378–390, 1995.

[34] J. Canny, "A computational approach to edge detection," *IEEE Transactions on Pattern Analysis and Machine Intelligence*, vol. 8, no. 6, pp. 679–698, 1986.

[35] D. W. Marquardt, "An algorithm for least-squares estimation of nonlinear parameters," *SIAM Journal on Applied Mathematics*, vol. 11, no. 2, pp. 431–441, 1963.

[36] "VXL—C++ Libraries for Computer Vision," July 2009, http://vxl.sourceforge.net.

[37] M.-M. Yau and S. N. Srihari, "A hierarchical data structure for multidimensional digital images," *Communications of the ACM*, vol. 26, no. 7, pp. 504–515, 1983.

[38] J. Chouteau, J. L. Lerat, R. Testa, B. Moyen, and S. A. Banks, "Effects of radiograph projection parameter uncertainty on TKA kinematics from model-image registration," *Journal of Biomechanics*, vol. 40, no. 16, pp. 3744–3747, 2007.

[39] E. Gronenschild, "Correction for geometric image distortion in the x-ray imaging chain: local technique versus global technique," *Medical Physics*, vol. 26, no. 12, pp. 2602–2616, 1999.

[40] E. Gronenschild, "The accuracy and reproducibility of a global method to correct for geometric image distortion in the X-ray imaging chain," *Medical Physics*, vol. 24, no. 12, pp. 1875–1888, 1997.

[41] S. Fantozzi, A. Cappello, and A. Leardini, "A global method based on thin-plate splines for correction of geometric distortion: an application to fluoroscopic images," *Medical Physics*, vol. 30, no. 2, pp. 124–131, 2003.

[42] "Virtual animation of the kinematics of the human for industrial, educational and research purposes," August 2009, http://www.ulb.ac.be/project/vakhum/public_dataset/public-data.htm.

[43] G. Wu, F. C. T. van der Helm, H. E. J. (DirkJan) Veeger, et al., "ISB recommendation on definitions of joint coordinate systems of various joints for the reporting of human joint motion—part II: shoulder, elbow, wrist and hand," *Journal of Biomechanics*, vol. 38, no. 5, pp. 981–992, 2005.

[44] R. H. Gong, P. Abolmaesumi, and J. Stewart, "A robust technique for 2D-3D registration," in *Proceedings the 28th Annual International Conference of the IEEE Engineering in Medicine and Biology*, pp. 1433–1436, New York, NY, USA, August-September 2006.